HHS Public Access

Author manuscript

IEEE ASME Trans Mechatron. Author manuscript; available in PMC 2022 February 01.

Published in final edited form as:

IEEE ASME Trans Mechatron. 2021 February ; 26(1): 369–380. doi:10.1109/tmech.2020.3020504.

A Surgical Robotic System for Treatment of Pelvic Osteolysis Using an FBG-Equipped Continuum Manipulator and Flexible Instruments

Shahriar Sefati [Member, IEEE],
Laboratory for Computational Sensing and Robotics, Johns Hopkins University, Baltimore, MD, USA, 21218

Rachel Hegeman,
Laboratory for Computational Sensing and Robotics, Johns Hopkins University, Baltimore, MD, USA, 21218; Johns Hopkins University Applied Physics Laboratory, Laurel, MD, USA

Farshid Alambeigi [Member, IEEE],
Johns Hopkins University during the completion of this work and he is currently with the Department of Mechanical Engineering, University of Texas at Austin, Austin, TX, USA, 78712

Iulian Iordachita [Senior Member, IEEE],
Laboratory for Computational Sensing and Robotics, Johns Hopkins University, Baltimore, MD, USA, 21218

Peter Kazanzides [Member, IEEE],
Laboratory for Computational Sensing and Robotics, Johns Hopkins University, Baltimore, MD, USA, 21218

Harpal Khanuja,
Department of Orthopedic Surgery, The Johns Hopkins Medical School, Baltimore, MD, USA, 21205

Russell H. Taylor [Life Fellow, IEEE],
Laboratory for Computational Sensing and Robotics, Johns Hopkins University, Baltimore, MD, USA, 21218

Mehran Armand [Member, IEEE]
Laboratory for Computational Sensing and Robotics, Johns Hopkins University, Baltimore, MD, USA, 21218; Johns Hopkins University Applied Physics Laboratory, Laurel, MD, USA; Department of Orthopedic Surgery, The Johns Hopkins Medical School, Baltimore, MD, USA, 21205

Abstract

This paper presents the development and experimental evaluation of a redundant robotic system for the less-invasive treatment of osteolysis (bone degradation) behind the acetabular implant during total hip replacement revision surgery. The system comprises a rigid-link positioning robot

Corresponding Author: Shahriar Sefati, address: 3400 N Charles St., Baltimore, MD, USA, 21218, sefati@jhu.edu, phone: +1(443)691-9322.

and a Continuum Dexterous Manipulator (CDM) equipped with highly flexible debriding tools and a Fiber Bragg Grating (FBG)-based sensor. The robot and the continuum manipulator are controlled concurrently via an optimization-based framework using the Tip Position Estimation (TPE) from the FBG sensor as feedback. Performance of the system is evaluated on a setup that consists of an acetabular cup and saw-bone phantom simulating the bone behind the cup. Experiments consist of performing the surgical procedure on the simulated phantom setup. CDM TPE using FBGs, target location placement, cutting performance, and the concurrent control algorithm capability in achieving the desired tasks are evaluated. Mean and standard deviation of the CDM TPE from the FBG sensor and the robotic system are 0.50 mm, and 0.18 mm, respectively. Using the developed surgical system, accurate positioning and successful cutting of desired straight-line and curvilinear paths on saw-bone phantoms behind the cup with different densities are demonstrated. Compared to the conventional rigid tools, the workspace reach behind the acetabular cup is 2.47 times greater when using the developed robotic system.

Keywords

Minimally-Invasive Surgery; Continuum Manipulator; Fiber Bragg Grating; Orthopedic Surgery

I. Introduction

ADVANCES in robot-assisted surgery have focused on minimizing the invasiveness of a given procedure while also maintaining an optimal outcome [1], [2]. To this end, Continuum Dexterous Manipulators (CDMs) and flexible robots have played a significant role in enhancing dexterity, workspace reach, and maneuverability in confined spaces during surgeries [3], [4], [5], [6]. Examples of the use of CDMs for these purposes can be found across surgical domains such as cardiac [7], abdominal [8], head and neck [9], [10], gastroscopy [11], endoscopic [12], [13], [14], and transnasal [15], [16]; most of which are concerned with soft environments. Orthopaedic surgeries, however, necessitate interaction with soft and hard tissues, therefore, the contact forces between the instruments and the body can be significantly higher.

We present the development and evaluation of a redundant surgical robotic system for orthopaedic interventions. The most important component of the system is a CDM developed specifically for orthopaedic applications [17], [18]. The CDM is equipped with a Fiber Bragg Grating (FBG)-based sensor for position estimation in real-time [19], [20], [21], [22], and is designed so that flexible debriding instruments may be inserted through the CDM's instrument channel [23], [24]. The CDM is mounted on a 6-Degree-Of-Freedom (DOF) rigid-link robot, resulting in a redundant robotic system.

In this paper, we focus on evaluating the system's performance in the surgical removal of osteolysis after total hip revision surgery. Osteolysis occurs due to the wear of the polyethylene liner that causes macrophage activation and osteolysis of the bone surrounding the implant (Fig. 1). Conventional treatment of osteolysis involves insertion of rigid instruments through the screw holes of the acetabular cup prosthesis. However, a review of the literature indicates that on average less than 50% of the lesion is removed with

conventional rigid instruments [25]. Robotic-assisted less-invasive treatment of osteolysis with the proposed system, on the other hand, leverages the high dexterity of the CDM and flexible debriding instruments to increase the surgeon's reach behind the cup, improving upon the conventional approach.

In the envisioned scenario for the robot-assisted less-invasive treatment of osteolysis, the combined robotic system will be concurrently controlled with FBG feedback to bring the tool's tip to desired target points, while the flexible instruments passed through the CDM debride the lesions. Appropriate virtual fixtures are incorporated into the control algorithm to avoid potential CDM collision with the cup and increase safety. It is worth noting that the key challenge of this procedure is the use of a CDM integrated with flexible cutting instruments to interact and accurately mill/drill the sclerotic wall (hardened tissue) surrounding the lesion.

The significant contributions reported in this paper are as follows: 1) development of a complete surgical robotic system aimed for the less-invasive treatment of pelvic osteolysis; 2) experimental study using the developed system and simulated bone phantoms (i.e. saw-bone samples); 3) evaluation of the overall system performance and accuracy of the individual components of the system such as FBG sensing capabilities, controller, and cutting performance; and 4) workspace comparison of the developed system to the conventional rigid tools.

II. Robotic System Components

The redundant robotic system (Fig. 2) is composed of a rigid-link positioning robot, a CDM with its actuation unit, flexible debriding instruments that are inserted into the CDM instrument channel, and an FBG-based sensing unit used for the real-time Tip Position Estimation (TPE) of the CDM.

A. Rigid-Link Robot

A 6-DOF rigid-link UR5 (Universal Robots, Inc., Odense, Denmark) is used for positioning of the CDM and its actuation unit in the proposed redundant system. The forward kinematics of this manipulator can be described by a mapping $g_R : \Theta \rightarrow SE(3)$, from joint variable space to end-effector configuration space. Using the product of exponentials formula:

$$g_R(\Theta) = \left(\prod_{i=1}^{6} e^{\hat{\xi}_i \Theta_i} \right) g_R^0 \tag{1}$$

where g_R^0 represents the rigid body transformation between the end-effector and base frames when the robot is in its reference configuration, and ξ_i is the twist coordinate for joint i on the robot. For a revolute joint, this twist has the form:

$$\xi_i = \begin{bmatrix} -\omega_i \times r_i \\ \omega_i \end{bmatrix} \tag{2}$$

where $\omega_i \in \mathbb{R}^3$ is a unit vector in the direction of the twist axis and $r_i \in \mathbb{R}^3$ is an arbitrary point on the axis of joint i. Considering (2), the robot Jacobian (J_R) can be computed as follows:

$$J_R(\Theta) = \left[\xi_1 \ \xi_2' \ \cdots \ \xi_6'\right]; \xi_i' = Ad_{(e^{\hat{\xi}}1\Theta_1 \ldots e^{\hat{\xi}}i-1\Theta_{i-1})}\xi_i \tag{3}$$

where Ad is the matrix of adjoint transformation depending on the configuration of the robot.

B. Continuum Dexterous Manipulator

The CDM used in the robotic system is constructed from a Nitinol (NiTi) tube with several notches to achieve flexibility and compliance in the direction of bending, while achieving high stiffness in the perpendicular direction to the plane of bending. The overall length of the flexible part of the CDM is 35 mm, with the Outside Diameter (OD) chosen as 6 mm so that it can pass through a screw hole of the acetabular implant. The CDM also contains a 4 mm instrument channel for insertion of different flexible debriding tools [23], [24]. As shown in Fig. 3(e), the CDM's wall contains four lengthwise channels for passing actuation cables and fiber optic sensors. The CDM fabrication procedure includes a wire EDM procedure where the lengthwise sensor and actuation channels are first generated on a piece of 35 mm NiTi tube, followed by another wire EDM procedure that creates the notches along the length of the tube (Fig. 3(d)) to provide the planar bending capability of the CDM. The bidirectional planar motion of the CDM is then achieved by actuating two cables embedded inside two channels (0.5 mm OD) along the length of the manipulator, one on each side of the CDM. For assembly, the cables are inserted from the proximal end (base) of the manipulator and passed through the channels all the way to the distal end (tip). The cables are knotted on the distal end so that pulling on the cables from the proximal end (by the actuation unit) causes the CDM to bend accordingly. The actuation cables are flexible braided wire ropes made of stainless steel (8930*T*16, McMaster-Carr) with 0.35 mm OD and nylon coating to avoid abrasion and reduce friction with the CDM channels.

C. Flexible Debriding/Cutting Instruments

Previous studies by our group have demonstrated successful soft tissue debridement [24]. The focus of this work, however, is on the harder problem of the removal of the sclerotic tissue (hard tissue). Fig. 3(c) shows a typical custom-designed and fabricated flexible debriding/cutting instrument to be inserted inside the CDM's 4 mm instrument channel for hard tissue removal. The end-mill head of this tool was chosen after studying the performance of different types of cutting tools designed for both side-cutting and drilling soft and hard saw-bone phantoms [23]. The tool consists of a rigid stainless steel tube (2.8 mm outer diameter), and a 3.5 mm flexible torque coil (Asahi Intec USA, Inc.) with 35 mm length. This torque coil provides sufficient torque to the tip of the tool, while it can adapt to various shapes of the CDM. A ball-end carbide end mill with a shaft diameter of 7 mm, two flutes and helix angle of 30 degree (8878*A*18, McMaster-Carr) has been glued to the flexible torque coil. To insert the cutter into the torque coil, we machined the end mill shaft to 2 mm length. From the surgical workflow perspective, the flexible instruments should contain the capability to be quickly interchanged according to the surgical plan and different phases of

the surgery. The decision on choosing a particular tool head size depends on the realization of the trade-off between larger lesion removal and easier integration with the CDM. For a fixed motion and contact with the specimen, a larger tool head can remove a greater chunk of the lesion, while a smaller tool head (less than 4 mm) can be easily interchanged and integrated during the surgery from the proximal side of the manipulator. Tool heads with OD below and above 4 mm could be inserted from the proximal and distal end of the actuation unit (and manipulator), respectively. Of note, the rigid shaft of the instrument is connected to the transmission system via a quick grip mechanism (shown in Fig. 3(a)).

D. FBG Sensor and Position Estimation Algorithm

1) Sensor Design and Fabrication: The FBG sensor used for this study has three FBG fibers attached to a flexible NiTi wire substrate with an OD of 0.5 mm in a triangular configuration (Fig. 3(e)). Three grooves (radially 120° apart from each other) are engraved by laser (Potomac, USA) along the length of the wire to hold three fibers each with three FBG nodes (Technica S.A, China). The fibers are glued into the engraved notches by applying epoxy glue (J-B Clear Weld Quick Setting Epoxy) under the microscope. Due to its relatively small OD, the NiTi wire can withstand curvatures of as small as 20 mm radius during bending, which is sufficient to cover and sense large deflections of the CDM [20]. Even though other sensor configurations with different numbers of fibers could potentially be used, three fibers can achieve 3-D shape reconstruction of the sensor [26] and provide temperature compensation capabilities. As compared to enclosed sensor substrates such as tubes with open lumens [19], the NiTi design in this study has the advantage of direct exposure to the grooves where the fibers are placed. As a result, the fabrication procedure and placement of the fibers are far easier compared to an enclosed substrate. For assembling the fabricated sensor into the CDM, the sensor is inserted into the sensor channel from the proximal side of the CDM and small amount of adhesive (J-B Cold-Weld Steel Reinforced Epoxy) is applied to attach the sensor and CDM from the distal end.

2) Data-driven Tip Position Estimation: The FBG sensor estimates the CDM tip position to serve as real-time feedback to the controller. More common shape sensing techniques using FBG involve finding the curvature at discrete FBG active areas and integrating curvature over the length of the CDM for TPE [26]. However, due to the limited number of sensing locations and many geometrical assumptions, these methods are prone to large error propagation especially when the CDM undergoes large deflections. In an effort to minimize the error in TPE, we previously proposed a model-independent data-driven approach that consisted of a regression model that was pre-operatively (off-line) trained on position information from the optical tracker as the ground truth [27]. During the training phase, the CDM cables are actuated to bend the manipulator to large curvatures, while a customized rigid body with four spherical markers is attached to the CDM tip. The data from the optical tracker and the FBGs are recorded and time-stamped for synchronization. This created data-set is used for training the tip position estimator regression model. The CDM tip position is then estimated intraoperatively (on-line) using only the FBG wavelength data and the preoperative trained model. Of note, for enhanced accuracy, CM actuation torque information could also be passed to the model as additional input. The used regression model is of the form:

$$p = \Psi(\lambda, \beta) \tag{4}$$

where $p \in \mathbb{R}^3$ is the 3-D position of the CDM tip, $\lambda \in \mathbb{R}^m$ is the vector containing the raw FBG wavelength data, β is the vector of unknown parameters, and Ψ is the regression model. The CDM TPE can be modeled as a least squares optimization problem:

$$\underset{B}{\operatorname{argmin}} \ \|\Lambda B - P\|_2^2 \tag{5}$$

where $\Lambda \in \mathbb{R}^{N \times m}$ is a stack of N observations of the m FBG node data, $P \in \mathbb{R}^{N \times 3}$ is the stack of N true CDM tip position observation data from the optical tracker, and $B \in \mathbb{R}^{m \times 3}$ is the matrix of unknown parameters. The unknown parameters B can be found during the pre-operative model training to estimate CDM tip position $\hat{p}_C$ with respect to the CDM base:

$$B = \left(\Lambda^T \Lambda\right)^{-1} \Lambda^T P; \quad \hat{p}_C = B^T \lambda \tag{6}$$

One concerning factor in the developed system is the effect of vibration caused by the debriding tools on the FBG sensor signal. In a previous work, this effect has been fully investigated [28]. According to that study, to reduce measurement uncertainties, a Butterworth low-pass filter is developed on top of the sensory data to reject the unwanted high frequency components of the received signal from the FBGs when the debriding tool is in use.

E. Actuation Unit

The system actuation unit (Fig. 3) contains two motors (RE16, Maxon Motor Inc.) with spindle drives (GP16, Maxon Motor, Inc.) to actuate the CDM cables. In addition, another DC motor (RE16, GP16C, Maxon Motor Inc.) rotates the actuation unit about its central axis (roll DOF) via a transmission belt for out-of-plane cutting and drilling capabilities. This actuation unit provides a central channel for insertion of the instruments, which are rotated with desired velocity by a DC motor (EC 22, GP22C, Maxon Motor Inc.) and a transmission and gripping mechanism. A custom C++ interface performs independent velocity or position control of the motors.

III. Control Method

The system contains a total of 9 DOFs: 6 DOFs from the rigid-link UR5 robot, 2 DOFs from the CDM, and 1 extra DOF from the actuation unit axial roll motion which rotates the CDM about its axial shaft for out-of-plane movements. The overall system's transformation chain and Jacobian from robot base to CDM tip can be written as:

$$\begin{aligned} x_{tip} &= g_R \cdot g_A \cdot \hat{p}_C \\ J_{system} &= \begin{bmatrix} J_R & J_A & J_C \end{bmatrix} \end{aligned} \tag{7}$$

where g and J refer to homogeneous transformation and Jacobian, and subscripts R, A, and C correspond to UR5 robot, actuation unit, and the CDM, respectively. g_R and J_R are known

from (1) and (3), given any set of UR5 robot joint angles. g_A is found from a hand-eye calibration step described in section IV-A. $\hat{p}_C$ is CDM tip with respect to its base and is found via FBG sensor data using the trained regression model from (6). x_{tip} is the CDM tip position described in the UR5 robot base frame (Fig. 2). J_A is known by incorporating the actuation roll joint variable in the kinematics of the rigid-link robot, and J_C is found by taking the Jacobian of the mapping between CDM cables' displacements and its tip position estimations. This mapping is found experimentally by actuating the CDM cables by known displacements and tracking the CDM tip position using the optical tracker. To achieve more accurate cable position estimation, backlash compensation methods could be deployed [29]. Alternatively, J_C can be estimated on-line adaptively [30]. It should be noted that $J_R \in \mathbb{R}^{6\times 6}$, $J_A \in \mathbb{R}^{6\times 1}$, $J_C \in \mathbb{R}^{6\times 2}$, and therefore $J_{system} \in \mathbb{R}^{6\times 9}$.

A. Concurrent Control Formulation

During robot-assisted treatment of osteolysis, all system components must be controlled concurrently to take advantage of the redundancy of the robotic system (more than six DOFs) and to bring the CDM tip to pre-operatively identified target points behind the cup. In doing so, several physical constraints (virtual fixtures) should be taken into account to ensure safe insertion and manipulation of the CDM into and behind the acetabular cup screw hole. We, therefore, utilize an optimization-based control framework which generates incremental actuation input for all the system's joints, given a desired target goal point and the current tip position of the CDM at each time step. All the physical and safety criteria for the robot-assisted treatment of osteolysis are incorporated into the controller by adding constraints to the optimization problem:

$$\begin{aligned} &\underset{dq^k}{\text{argmin}} \quad \left\| dx_{obj}^k - J_{system}^k dq^k \right\| \\ &\text{subject to} \;\; Physical\ Constraints \end{aligned} \tag{8}$$

where the *Physical Constraints* are formulated in section III-B, dx_{obj}^k is the objective Cartesian CDM tip position displacement at time step k to reach a desired goal point, and $q^k \in \mathbb{R}^9$ is the state of the system at this time step, and is formed by concatenating the 9 joint input variables from UR5, actuation unit roll motion, and the CDM actuation cable lengths:

$$q = \left[\theta_{R1} \;\ldots\; \theta_{R6} \;\theta_A \;l_{C1} \;l_{C2}\right] \tag{9}$$

where θ_{Ri} refers to i^{th} UR5 robot revolute joint, θ_A refers to the axial roll motion angle on the actuation unit, and l_{Ci} corresponds to i^{th} cable displacement on the CDM. The desired output in Cartesian coordinates is defined and regulated via a PD controller to avoid possible overshoot and enhance stability, and then passed to the optimizer (8):

$$\begin{aligned} dx_{des}^k &= x_{goal}^k - x_{tip}^k \\ dx_{obj}^k &= k_p dx_{des}^k + k_d \frac{dx_{des}^k}{dt} \end{aligned} \tag{10}$$

where k_p and k_d are proportional and derivative gains, respectively, x_{tip}^k is computed from (7) at time step k, and x_{goal}^k is the next surgical target goal point at time step k.

The concurrent control optimization problem works as follows: at time step k, given the current state of the system (q^k), the system Jacobian (J_{system}^k) is computed via (7). The current tip position of the CDM (x_{tip}^k) is found using the FBG sensor raw wavelength data and (6). Given the desired target point (x_{goal}^k), the objective displacement at this time step (dx_{tip}^k) can therefore be computed using (10) and passed to the optimizer. As a result, the incremental system joint inputs (dq^k) are generated to bring the CDM tip to the target goal point. A small threshold (such as γ) is specified as the termination threshold of the algorithm. In other words, the system control inputs are generated via (8) until dx_{des} becomes less than γ. The system's closed-loop control diagram is shown in Fig. 4.

B. Physical Constraints Formulation

As mentioned, robot-assisted treatment of osteolysis involves physical constraints that should be satisfied during the system concurrent control. Each of these constraints can be modeled mathematically and incorporated into the first step of the concurrent control optimization problem (8). Here we describe and model these physical and safety constraints in detail:

1) RCM Constraint: The acetabular cup screw hole is the point of entry for the CDM, and therefore is considered as the Remote Center of Motion (RCM) for the system, denoted by p_{RCM}, meaning that the system must always intersect the cup at this point for successful operation as well as patient safety. We also define $p_{closest}$ as the intersection of the central shaft of the actuation unit and the virtual plane passing through the screw hole with the axis of the screw hole as normal to the plane. Near the RCM point, the shaft must stay within a virtual cylinder defined by the axis and radius of the screw hole. This cylinder can be approximated by a prism with n faces (Fig. 5). The goal is to ensure the generated joint input from (8) at time step k, will move the system such that $p_{closest}^{k+1}$ remains within the prism:

$$v_i \cdot \left(p_{closest}^{k+1} - p_{RCM}\right) < \epsilon, \quad for\ \forall i \in 1, \ldots, n \tag{11}$$

where v_i refers to the unit vector normal to the i^{th} face of the prism. With some manipulation of (11), we can relate this constraint to the Jacobian of the closest point ($p_{closest}$):

$$\begin{aligned} &v_i \cdot \left(p_{closest}^{k+1} - p_{closest}^k - p_{RCM} + p_{closest}^k\right) < \epsilon \Rightarrow \\ &v_i \cdot \left(dp_{closest}\right) < \epsilon + v_i \cdot \left(p_{RCM} - p_{closest}^k\right) \Rightarrow \\ &v_i \cdot \left(J_{closest} dq_R\right) < \epsilon + v_i \cdot \left(p_{RCM} - p_{closest}^k\right) \end{aligned} \tag{12}$$

and stacking the n constraints together:

$$H * (J_{closest} dq_R) < E + H * \left(p_{RCM} - p^k_{closest}\right)$$
$$where:\ H = \left[v_1\ v_2\ \dots\ v_n\right]^T \quad (13)$$
$$E = \underbrace{[\epsilon\ \dots\ \epsilon]}_{n\ times}$$

2) Stay Near Axis Constraint: To ensure patient safety, we bound the end shaft of the surgical system to move only within a desired conical workspace around a desired axis ($axis_{des}$) which is chosen as the screw hole axis (axis normal to the acetabular cup). This constraint is formulated as follows:

$$axis_{des} \cdot \underbrace{(axis_{cur} + J^{\omega}_{base} dq_R)}_{Next\ Step's\ Axis} \geq \cos(\theta_{threshold}) \quad (14)$$

where J^{ω}_{base} corresponds to the angular component of the Jacobian resolved at the base of the CDM, and $axis_{cur}$ and $axis_{des}$ refer to the current and desired end shaft of the robot, respectively. $\theta_{threshold}$ is the maximum deviation angle allowed from $axis_{des}$.

3) Joint Constraints: To ensure safe manipulation of the system, joint positions and velocities are constrained to avoid potential damage to the system due to collision, actuation cable damage, etc. These constraints can be formulated as:

$$dq > q_{lower} - q,\ -dq > -q_{upper} + q$$
$$dq > q_{v,l},\ -dq > -q_{v,u} \quad (15)$$

All derived final non-equality formulas in (13), (14), and (15) are substituted for *Physical Constraints* in the first optimization step of the controller (8). Further information on these constraints could be found in [31].

IV. Pre-operative Preparations

A. Hand-Eye Calibration

To complete the forward kinematics of the system, the relationship between the robotic system (hand) and the optical tracker (eye) must be known. More specifically, the transformation associated with the actuation unit, g_A (transformation between UR5's end-effector and the base of the CDM), as well as the transformation between the world reference geometry and the base of the UR5 robot (g_w) are obtained by performing a hand-eye calibration. The chain of transformations is closed by attaching a custom-designed reference geometry into the CDM instrument channel (Fig. 2) and reading the transformation between this geometry and the world reference geometry (g_c). The UR5 robot is then moved arbitrarily to a few different poses and g_c is obtained using a Polaris (Northern Digital Inc., Waterloo, Canada) optical tracker, while g_R is known from the robot's forward kinematics. The hand-eye calibration problem is formulated as follows:

$$g_R g_A = g_w g_c \tag{16}$$

To solve this problem, the unknown g_w is written with respect to g_A by taking an observation from the optical tracker:

$$g_w = g_R^0 g_A \left(g_c^0\right)^{-1} \tag{17}$$

Substituting (17) in (16) and rearranging:

$$\underbrace{\left(g_R^0\right)^{-1} g_R}_{A} \underbrace{g_R}_{X} = \underbrace{g_A}_{X} \underbrace{\left(g_c^0\right)^{-1} g_c}_{B} \tag{18}$$

which is the conventional $AX = XB$ problem. The solution for g_A can then be substituted in (16) to solve for g_w.

B. Acetabular Cup Localization

A digitizing tool with spherical markers attached to its body is used to localize the acetabular cup screw hole. This is done by performing a pivot calibration about the screw hole (RCM point). Once the the tool geometry is known from the pivot calibration, the axis of the screw hole ($axis_{des}$) is found by digitizing the rim of acetabular cup and computing the normal vector of the plane that fits through these digitized points by setting up a least squares problem.

C. Osteolytic Lesion Localization

A similar procedure to that described in section IV-B is performed to trace the desired target points to be removed by the system from behind the cup. The collected points serve as a 3D model of the target points that the CDM tip will follow and the debriding instruments will remove from the phantom. It is worth noting that in the clinical scenario, these target points will be identified from the pre-operative patient CT. Consequently, no digitizing of the target points behind the cup will be necessary in such setting.

V. Experiment Design and Evaluation Criteria

To mimic the real scenario of robot-assisted treatment of osteolysis, we designed and fabricated experimental phantoms from hard saw-bone material (made of polyurethane) with different hardness (Pacific Research Laboratories, USA), since they offer uniform and consistent physical properties in the range of human bone and are, therefore, suitable for biomechanical studies [32]. In particular, two different saw-bone phantoms with 10 and 15 Pounds per Cubic Foot (PCF) densities (corresponding to 160.18 and 240.28 kg/m^3, respectively) were used. The phantoms were placed behind a 3D printed acetabular cup component with realistic dimensions to evaluate the cutting performance of the system.

We carried out various experiments to evaluate the performance of the system with respect to different criteria: 1) CDM compliance analysis, 2) CDM tip estimation accuracy (for the

FBG sensor and the whole system), 3) controller performance in successful tracking of the goal points, 4) workspace comparison between the developed surgical robotic system and conventional rigid tools when reaching behind the acetabular cup, and 5) hard bone removal capability from the saw-bone phantom behind the acetabular cup and cutting performance in different digitized (random) or generated desired surgical goal points (such as line or curve).

To evaluate the CDM tip estimation accuracy from FBGs, we attached a custom-designed rigid body to the tip of the CDM, which was tracked by the optical tracker with respect to the base of the CDM (Fig. 2). This data served as the ground truth CDM tip position for performance evaluation of the data-driven approach described in section II-D2. To ensure the feasibility of using the proposed system for simultaneous concurrent controlling of CDM to target points and cutting, we evaluated the controller's performance in tracking various goal trajectories such as randomized curvilinear paths, straight lines, and arcs, with different spacing of the consecutive points on the trajectory. To simulate different parts of bone and the osteolytic lesions behind the acetabular cup, we evaluated the performance of the system in removing desired goal points from simulated hard bone phantoms with different densities.

VI. Results

A. CDM Compliance Analysis

To determine the maximum distal-end force, perpendicular to the bending plane, that the CDM can sustain before breaking, the CDM was rigidly fixated on an actuation unit while the actuation cables were counter-tensioned to 4.00 N to hold the CDM firmly at the straight configuration (Fig. 6(a)). A three-axis force sensor (OMD-10-SE-10N, OptoForce; Budapest, Hungary) was mounted on a linear stage and brought downward slowly until the CDM was ruptured from the proximal end. As demonstrated in Fig. 6(c), a maximum force of 11.54 N was observed before occurrence of rupture. This value is sufficient for contact forces observed during debridement of hard simulated bone and soft tissue [23], [24]. Sustaining such a large out-of-plane distal end force is one of the unique features of this particular CDM, making it a great candidate for orthopaedic interventions. Moreover, for the bending plane forces, Kutzer et al. [18] previously reported end-effector reaction forces as large as nearly 2.00 N while the CDM cables were actuated to push the manipulator against a load cell placed at the distal end of the manipulator.

B. Tip Position Estimation Accuracy

1) CDM TPE Accuracy: The FBG sensing unit incorporated into the CDM estimates the tip position with respect to the CDM base. The accuracy of the system therefore depends on how well the FBG sensor can estimate the CDM tip position. Figs. 7(a), (b), and (c) indicate the predicted and the ground truth CDM tip position in the two dimensions on the bending plane separately, as well as the resulting feedback on the plane. The regression model from section II-D2 predicted the TPE using only the FBG sensing data and the results were compared to ground truth data from the optical tracker. The mean and standard deviation of the CDM tip tracking error are 0.11 mm, and 0.07 mm, respectively, with maximum error of 0.37 mm. This ensures accurate TPE for the CDM with respect to the base of the CDM.

2) System TPE Accuracy: Using the estimated CDM tip position with respect to its base, and the transformations obtained from the hand-eye calibration procedure described in section IV-A, the CDM tip position can be obtained with respect to the base of the entire robotic system, which would then be used as tip position feedback into the controller (x_{tip} in (7)). The results of the system TPE are compared to the ground truth tip positions from a custom-designed optical tracker rigid body attached to the CDM tip. Fig. 7(d) demonstrates these results during various concurrent motions of the entire robotic system, where the CDM is bent to maximum curvatures associated with radius of curvature as small as 20 mm. The mean and standard deviation of the entire system tip tracking error are 0.50 mm, and 0.18 mm, respectively, with maximum error of 1.46 mm. Such precision in TPE for the system provides accurate real-time feedback to the controller when bringing the system tip position to the desired surgical points.

C. Controller Performance

To ensure safe manipulation of the robotic system during surgery, k_p and k_d gains of the controller were chosen to avoid any overshoot in placement of the CDM tip on target points (0.4 and 0.1, respectively). A desired adjustable threshold determines how close the CDM tip position should get to a particular goal point in order for the controller to mark the goal point as reached. A threshold of 1 mm for the controller's stopping criterion is reasonable for orthopedic applications and particularly osteolysis, since the goal is to remove a volume of lesion/bone behind the acetabular cup. Fig. 8(a) demonstrates the controller's successful performance when moving the system's tip position between corners of a cube in space with 100 mm length edges. This figure shows the ground truth and the tracked CDM tip position computed with respect to the base of the entire system, using the FBG sensor combined with the forward kinematics of the robot. Fig. 8(b) demonstrates the controller's successful performance in reaching the goal points on straight trajectories without overshoot, when tracing the edges of the cube in the order and directions shown in Fig. 8(a).

The controller was also evaluated on curved paths, e.g. a circle. Figs. 9(a) and 9(b) demonstrate the performance of the controller when tracing a circle behind the acetabular cup component, with active and inactive optimization constraints. Even though the feasible region for the optimization solution search-space is limited when the constraints are activated, the controller is still capable of tracing the circular path behind the cup successfully. Figs. 9(c) and 9(d) show the distance between the CDM tip position and the current goal point over the course of the entire trajectory. The mean and standard deviation of this distance are 1.33 mm, 0.37 mm, with maximum distance of 1.94 mm, when the constraints are inactive, and 1.52 mm, 0.42 mm, with maximum distance of 2.98 mm, when the constraints are active. Table I summarizes these results. In addition, the CDM tip velocity during the control procedure is demonstrated in Figs. 9(e) and 9(f). This velocity is measured by transforming the generated joint-space velocities ($\dot{q}$) to the task-space ($\dot{x}_{tip}$) using the combined system Jacobian ($\dot{x}_{tip} = J\dot{q}$). The generated joint-space velocities from the optimization framework depend on the bounds for the allowed velocities from section III-B3. The robotic system contains long links resulting in relatively large motion of the CDM tip even for small joint motions. Therefore, for safe manipulation inside the patient's body the UR5 joint velocities had to be limited to obtain optimal cutting performance. After

running experiments to achieve optimal performance, we limited the UR5 joint velocities to [0.002 0.002 0.002 0.001 0.002 0.001] rad/sec. These velocity limits are, however, adjustable before and during the motion and can be set by the user accordingly. The mean (and standard deviation) generated task-space velocity is 4.06 (2.28) mm/s, and 3.31 (1.59) mm/s, when the constraints are active and inactive, respectively. The larger mean distance from goal points and higher mean velocity with active constraints is associated with the larger deviations from the desired path (as can be seen by comparing Figs. 9(a) and 9(b)) due to the constraints imposed on the controller. The controller is doing the best possible to bring the CDM tip closer to the next goal points, however, the constraints may hinder the controller from moving the CDM tip directly toward the goal points. As such, the controller generates commands that result in CDM tip motions with projection components in the direction toward the goal points. As a result, slightly larger mean distance from goal points and higher mean velocity for the CDM tip is observed when the constraints are active.

D. Experimental Workspace Analysis

Conventional treatment of osteolysis involves insertion of rigid instruments through the screw holes of the acetabular cup component. Using the same screw hole on the acetabular cup component, we have measured and compared the workspace achieved by a conventional rigid instrument and the developed surgical robotic system experimentally, when running the system with the maximum physical bounds, such as the maximum allowed CDM cable lengths. Fig. 10 demonstrates the maximum reach behind the cup for each approach by comparing a cross section of the covered workspace. The complete workspace is achieved by revolving these cross sections about the axis of the screw hole. The workspace volume associated with the conventional and the robot-assisted treatment approaches are 17462 mm^3 and 43084 mm^3, respectively. The proposed robotic system would therefore cover 2.47 times more workspace volume as compared to rigid instrument treatment of osteolysis.

E. Cutting Performance

Fig. 11 shows the performance of the system in navigating the CDM tip position to goal points on desired paths within the workspace of the robotic system (within the blue region in Fig. 10, not reachable thoroughly by rigid tools) consisting of curvilinear and straight-line segments (described in section V) while the flexible debriding tool is cutting the phantom surfaces with two different densities (10 and 15 PCF). The desired target trajectories, as well as the traversed system tip position during the procedures are shown in Figs. 11(a) and 11(e). In addition, the preoperative data obtained from the calibration step such as the RCM point, and the acetabular cup rim digitized points, all described with respect to the rigid-link robot's coordinate frame are demonstrated in these figures.

An important aspect of the cutting performance is the velocity with which the flexible tool sweeps the cutting surface (task-space velocity). This velocity is especially important since the system is designed to cut simulated hard bone. We incorporated a velocity percentage parameter in the user interface to allow users to adjust a fraction of the task-space velocity for cutting. Figs. 11(b) and 11(f) show the generated task-space velocity for 50% and 80% velocity percentages during cutting, respectively. The mean and standard deviation of the task-space velocity are 2.43 mm/s, and 0.93 mm/s for the 50% ratio, and 3.94 mm/s, and

1.15 mm/s for the 80% ratio. Figs. 11(c) and 11(g) report the CDM tip distance to target goal points for the entire duration of the cutting experiments. Table I summarizes these distance results and compares them with the free environment motion distances. The resulting cut surface for the saw-bone phantoms with PCF 10 and 15 are demonstrated in Figs. 11(d) and 11(h), respectively. The mean measured cutting volume rate over time for material removal was measured at 0.0083 mm^3/s. Additionally, Fig. 12 demonstrates snapshots of the system during cutting of the PCF 10 saw-bone phantom behind the acetabular cup.

VII. Discussion

One of the most important attributes of a surgical robotic system is the ability to provide accurate feedback with high frequency. The developed system integrates our non-constant curvature CDM with an FBG sensing unit with the ability to measure high curvatures and a data-driven algorithm for highly-accurate TPE real-time measurement. The system demonstrates sub-millimeter accuracy for the mean TPE of the CDM component alone, as well as for the entire system. Achieving such accuracy for CDMs with high curvatures (small radius of curvature) similar to the one used in this study is challenging, but the proposed data-driven approach estimates TPE accurately since it does not rely on any particular assumption regarding the sensor or CDM geometry. Rather, all the unknown parameters are implicitly captured from the data and incorporated in the data-driven model.

Several strategies could be deployed to further improve the TPE from the FBG sensors. The data-driven approach in this study was trained using only pre-operative data, whereas in practice, the ground truth CDM shape can be obtained from an X-ray image to refine and tune the data-driven model parameters intra-operatively. Moreover, the data-driven method predictions could be fused with the model-based approaches [26] to reduce statistical noises and other inaccuracies. As an alternative to FBGs, distributed high spatial resolution sensing based on optical frequency domain reflectometry could be used for TPE [33] to capture inflection points in reconstructing complex shapes (e.g. during interactions with obstacles). Multicore fibers with more inscribed FBGs can also potentially increase the sensing accuracy. The actuation unit mechanical design could be further improved to reduce vibrations and consequently sensor noise. Additionally, pre-tensioning CDM cables can reduce unwanted CDM motions due to vibration.

The generated joint velocity commands from each optimization iteration depend on the feasible region determined by the constraints that are active in the optimization problem. In the osteolysis application, certain constraints such as the RCM, and the joints' position and velocity bounds are crucial and should be active at all times. For instance, a violation from the RCM constraints would damage the CDM, and too fast or too slow joint velocities could result in suboptimal cutting performance. Other constraints such as the stay near axis may be relaxed or inactivated in a phantom experimental setup such as this study. These constraints are, nonetheless, advantageous or even required in a practical surgical setting and must be adjusted depending on the specific surgical procedure and hardware limitations. During the surgery, the allowed (and required) range of motion from the rigid-link robot is determined by the patient's incision length and the range of required workspace behind the cup.

The proposed system demonstrated successful removal of target points with two different task-space velocities on simulated hard bone phantoms with two different densities. A smaller generated task-space velocity may be chosen for the initial round of material removal or when there is expectation of harder materials presence. It was also shown that the workspace reached by the developed robotic system was 2.47 times greater than that of the conventional rigid tools. Of note, when the CDM is straight, the robotic system will also replicate what can be achieved by the rigid tools; i.e. the robotic system workspace is a super-set of the rigid tools' workspace. In the experiments, the joint limit for the CDM's actuation cable motor was set to 5 mm maximum displacement to avoid damage to the CDM. The workspace of the robotic system, however, can be increased by relaxing the joint limit constraints on the CDM to allow for higher bends. Moreover, other CDM lengths can be designed to cover a larger space behind the cup. Of note, the actuation unit roll joint range was not physically limited, as long as enough slack was accounted for the motor controller and FBG cables.

VIII. Conclusion

We have developed a redundant surgical robotic system for orthopaedic applications. The system exhibits flexibility and dexterity for applications that conventional rigid tools and instruments cannot perform optimally. System components' mechanical design, control and sensing algorithms, and the system integration were described. In addition, the developed system was tested in the robotic-assisted less-invasive treatment of osteolysis behind the acetabular implant during total hip arthroplasty revision surgery with a 2.47 times increase in the workspace compared to conventional rigid tools.

This study presented the development and evaluation of different system's components during the removal of hard tissue simulated phantoms behind the acetabular implant. While all the technical development presented in this study could be used in a clinical procedure as well, we will perform experiments on cadaver specimens in future work to tune the system further toward a clinical application.

Acknowledgment

The authors would like to gratefully acknowledge Dr. Ryan Murphy, Mr. Paul Wilkening and Mr. Zhibin Sun for their help with the system development.

Research supported by NIH/NIBIB grant R01EB016703 and Johns Hopkins University internal funds.

Biographies

Shahriar Sefati received his M.S.E. in Computer Science and Ph.D. in Mechanical Engineering from the Johns Hopkins University in 2017 and 2020, respectively. He has been

a member of the Biomechanical- and Image-Guided Surgical Systems (BIGSS) Laboratory, as part of the Laboratory for Computational Sensing and Robotics (LCSR), where he is currently serving as a postdoctoral researcher at the Autonomous Systems, Control, and Optimization (ASCO) laboratory. Prior to joining Johns Hopkins, he received his B.Sc. in Mechanical Engineering from Sharif University of Technology, Tehran, Iran, in 2014. His research interests include robotics and artificial intelligence for development of autonomous systems.

Rachel Hegeman received her M.S.E. in Computer Science from Johns Hopkins University in 2019, and worked for the Research and Exploratory Development Department at the Johns Hopkins Applied Physics Laboratory while assisting with this paper. She received a B.S. in Mechanical Engineering and a B.S. in Applied Math from the Johns Hopkins University in 2016. Her work mainly consists of developing novel robotic systems to accomplish important tasks in medicine, defense, and marine application areas. She now works as a robotics software engineer for Waymo LLC on their self-driving car system.

Farshid Alambeigi received his M.S.E. in Robotics and Ph.D. in Mechanical Engineering from the Johns Hopkins University in 2017 and 2019, respectively. Prior to joining Johns Hopkins, he received his B.Sc. and M.Sc. degrees in Mechanical Engineering from the K.N. Toosi University of Technology and Sharif University of Technology, Tehran, Iran, in 2009 and 2012, respectively. He is currently an Assistant Professor in the Department of Mechanical Engineering at the University of Texas at Austin. His research interests include development, sensing, and control of high dexterity continuum manipulators, soft robots, and flexible instruments especially designed for less-invasive treatment of various medical applications.

Iulian Iordachita (IEEE M08, S14) is a faculty member of the Laboratory for Computational Sensing and Robotics, Johns Hopkins University, and the director of the Advanced Medical Instrumentation and Robotics Research Laboratory. He received the

M.Eng. degree in industrial robotics and the Ph.D. degree in mechanical engineering in 1989 and 1996, respectively, from the University of Craiova. His current research interests include medical robotics,image guided surgery, robotics, smart surgical tools, and medical instrumentation.

Peter Kazanzides received the Ph.D. degree in electrical engineering from Brown University, Providence, RI, in 1988 and started working on surgical robotics as a Postdoctoral Researcher at the IBM T.J. Watson Research Center. He co-founded Integrated Surgical Systems (ISS) in November 1990 to commercialize the robotic hip replacement research performed at IBM and the University of California, Davis, as the ROBODOC System, which has been used for more than 20,000 hip and knee replacement surgeries. He joined the Engineering Research Center for Computer Integrated Surgical Systems and Technology (CISST ERC) in December 2002, where he is currently a Research Professor of Computer Science at The Johns Hopkins University, Baltimore, MD. His research interests include medical robotics, space robotics, and augmented reality.

Harpal Khanuja received BASc from University of Pennsylvania, MD from Albany Medical College, and completed residency in orthopaedic surgery with Albany Medical Center, and fellowship in adult joint reconstruction with Johns Hopkins University in 1991, 1995, 2000, and 2001 respectively. He is currently an Associate Professor and Chief of Adult Reconstruction in the Department of Orthopaedic Surgery at the Johns Hopkins University School of Medicine as well as Chair of the Department of Orthopaedic surgery at the Johns Hopkins Bayview Medical Center. His current research interests include primary and revision hip and knee arthroplasty surgery as well as treatment of osteonecrosis, osteolysis, and osteopororsis

Russell H. Taylor received the Ph.D. degree in computer science from Stanford University, in 1976. After working as a Research Staff Member and Research Manager with IBM Research from 1976 to 1995, he joined Johns Hopkins University, where he is the John C.

Malone Professor of Computer Science with joint appointments in Mechanical Engineering, Radiology, and Surgery, and is also the Director of the Engineering Research Center for Computer-Integrated Surgical Systems and Technology and the Laboratory for Computational Sensing and Robotics. He is an author of over 500 peer-reviewed publications and has 80 US and International patents.

Mehran Armand received Ph.D. degrees in mechanical engineering and kinesiology from the University of Waterloo, Ontario, Canada. He is a Professor of Orhtopaedic Surgery and Research Professor of Mechanical Engineering at the Johns Hopkins University (JHU) and a principal scientist at the JHU Applied Physics Laboratory. Prior to joining JHU/APL in 2000, he completed postdoctoral fellowships at the JHU Orthopaedic Surgery and Otolaryngology-head and neck surgery. He currently directs the laboratory for Biomechanical- and Image-Guided Surgical Systems (BIGSS) at JHU Whiting School of Engineering. He also co-directs the AVECINNA Laboratory for advancing surgical technologies, located at the Johns Hopkins Bayview Medical Center. His lab encompasses research in continuum manipulators, biomechanics, medical image analysis, and augmented reality for translation to clinical applications of integrated surgical systems in the areas of orthopaedic, ENT, and craniofacial reconstructive surgery.

References

[1]. Vitiello V, Lee S-L, Cundy TP, and Yang G-Z, “Emerging robotic platforms for minimally invasive surgery,” IEEE reviews in biomedical engineering, vol. 6, pp. 111–126, 2012. [PubMed: 23288354]

[2]. Ebrahimi A, Patel N, He C, Gehlbach P, Kobilarov M, and Iordachita I, “Adaptive control of sclera force and insertion depth for safe robot-assisted retinal surgery,” in 2019 International Conference on Robotics and Automation (ICRA). IEEE, 2019, pp. 9073–9079.

[3]. Burgner-Kahrs J, Rucker DC, and Choset H, “Continuum robots for medical applications: A survey,” IEEE Transactions on Robotics, vol. 31, no. 6, pp. 1261–1280, 2015.

[4]. Tamadon I, Huan Y, de Groot AG, Menciassi A, and Sinibaldi E, “Positioning and stiffening of an articulated/continuum manipulator for implant delivery in minimally invasive surgery,” The International Journal of Medical Robotics and Computer Assisted Surgery, vol. 16, no. 2, p. e2072, 2020. [PubMed: 31876096]

[5]. Chikhaoui MT, Lilge S, Kleinschmidt S, and Burgner-Kahrs J, “Comparison of modeling approaches for a tendon actuated continuum robot with three extensible segments,” IEEE Robotics and Automation Letters, vol. 4, no. 2, pp. 989–996, 2019.

[6]. Zhang Z, Dequidt J, Back J, Liu H, and Duriez C, “Motion control of cable-driven continuum catheter robot through contacts,” IEEE Robotics and Automation Letters, vol. 4, no. 2, pp. 1852–1859, 2019.

[7]. Gosline AH, Vasilyev NV, Butler EJ, Folk C, Cohen A, Chen R, Lang N, Del Nido PJ, and Dupont PE, “Percutaneous intracardiac beating-heart surgery using metal mems tissue approximation tools,” The International journal of robotics research, vol. 31, no. 9, pp. 1081–1093, 2012. [PubMed: 23750066]

[8]. Dwyer G, Chadebecq F, Amo MT, Bergeles C, Maneas E, Pawar V, Vander Poorten E, Deprest J, Ourselin S, De Coppi P et al., "A continuum robot and control interface for surgical assist in fetoscopic interventions," IEEE robotics and automation letters, vol. 2, no. 3, pp. 1656–1663, 2017. [PubMed: 28680967]

[9]. Schneider JS, Burgner J, Webster RJ III, and Russell PT III, "Robotic surgery for the sinuses and skull base: What are the possibilities and what are the obstacles?" Current opinion in otolaryngology & head and neck surgery, vol. 21, no. 1, p. 11, 2013. [PubMed: 23299117]

[10]. Wang H, Wang X, Yang W, and Du Z, "Design and kinematic modeling of a notch continuum manipulator for laryngeal surgery," International Journal of Control Automation and Systems, 2020.

[11]. Campisano F, Remirez AA, Landewee CA, Calò S, Obstein KL, Webster RJ III, and Valdastri P, "Teleoperation and contact detection of a waterjet-actuated soft continuum manipulator for low-cost gastroscopy," IEEE Robotics and Automation Letters, 2020.

[12]. Ma X, Song C, Chiu PW, and Li Z, "Autonomous flexible endoscope for minimally invasive surgery with enhanced safety," IEEE Robotics and Automation Letters, vol. 4, no. 3, pp. 2607–2613, 2019.

[13]. Hwang M and Kwon D-S, "Strong continuum manipulator for flexible endoscopic surgery," IEEE/ASME Transactions on Mechatronics, vol. 24, no. 5, pp. 2193–2203, 2019.

[14]. Zhang X, Li W, Chiu PWY, and Li Z, "A novel flexible robotic endoscope with constrained tendon-driven continuum mechanism," IEEE Robotics and Automation Letters, vol. 5, no. 2, pp. 1366–1372, 2020.

[15]. Burgner J, Rucker DC, Gilbert HB, Swaney PJ, Russell PT, Weaver KD, and Webster RJ, "A telerobotic system for transnasal surgery," IEEE/ASME Transactions on Mechatronics, vol. 19, no. 3, pp. 996–1006, 2013. [PubMed: 25089086]

[16]. Li C, Gu X, Xiao X, Lim CM, and Ren H, "Flexible robot with variable stiffness in transoral surgery," IEEE/ASME Transactions on Mechatronics, vol. 25, no. 1, pp. 1–10, 2019.

[17]. Murphy RJ, Kutzer MD, Segreti SM, Lucas BC, and Armand M, "Design and kinematic characterization of a surgical manipulator with a focus on treating osteolysis," Robotica, vol. 32, no. 6, pp. 835–850, 2014.

[18]. Kutzer MD, Segreti SM, Brown CY, Armand M, Taylor RH, and Mears SC, "Design of a new cable-driven manipulator with a large open lumen: Preliminary applications in the minimally-invasive removal of osteolysis," in 2011 IEEE International Conference on Robotics and Automation. IEEE, 2011, pp. 2913–2920.

[19]. Sefati S, Alambeigi F, Iordachita I, Armand M, and Murphy RJ, "Fbg-based large deflection shape sensing of a continuum manipulator: Manufacturing optimization," in 2016 IEEE SENSORS. IEEE, 2016, pp. 1–3.

[20]. Sefati S, Pozin M, Alambeigi F, Iordachita I, Taylor RH, and Armand M, "A highly sensitive fiber bragg grating shape sensor for continuum manipulators with large deflections," in 2017 IEEE SENSORS. IEEE, 2017, pp. 1–3.

[21]. Sefati S, Sefati S, Iordachita I, Taylor RH, and Armand M, "Learning to detect collisions for continuum manipulators without a prior model," in International Conference on Medical Image Computing and Computer-Assisted Intervention. Springer, 2019, pp. 182–190.

[22]. Ebrahimi A, He C, Roizenblatt M, Patel N, Sefati S, Gehlbach P, and Iordachita I, "Real-time sclera force feedback for enabling safe robot-assisted vitreoretinal surgery," in 2018 40th Annual International Conference of the IEEE Engineering in Medicine and Biology Society (EMBC). IEEE, 2018, pp. 3650–3655.

[23]. Alambeigi F, Wang Y, Sefati S, Gao C, Murphy RJ, Iordachita I, Taylor RH, Khanuja H, and Armand M, "A curved-drilling approach in core decompression of the femoral head osteonecrosis using a continuum manipulator," IEEE Robotics and Automation Letters, vol. 2, no. 3, pp. 1480–1487, 2017.

[24]. Alambeigi F, Sefati S, Murphy RJ, Iordachita I, and Armand M, "Design and characterization of a debriding tool in robot-assisted treatment of osteolysis," in 2016 IEEE International Conference on Robotics and Automation (ICRA). IEEE, 2016, pp. 5664–5669.

[25]. Engh CA Jr, Egawa H, Beykirch SE, Hopper RH Jr, and Engh CA, “The quality of osteolysis grafting with cementless acetabular component retention.” Clinical Orthopaedics and Related Research (1976-2007), vol. 465, pp. 150–154, 2007.

[26]. Roesthuis RJ, Kemp M, van den Dobbelsteen JJ, and Misra S, “Three-dimensional needle shape reconstruction using an array of fiber bragg grating sensors,” IEEE/ASME transactions on mechatronics, vol. 19, no. 4, pp. 1115–1126, 2013.

[27]. Sefati S, Hegeman R, Alambeigi F, Iordachita I, and Armand M, “Fbg-based position estimation of highly deformable continuum manipulators: Model-dependent vs. data-driven approaches,” in Medical Robotics (ISMR), 2019 International Symposium on, 2018, pp. 1–6.

[28]. Sefati S, Alambeigi F, Iordachita I, Taylor RH, and Armand M, “On the effect of vibration on shape sensing of continuum manipulators using fiber bragg gratings,” in 2018 International Symposium on Medical Robotics (ISMR). IEEE, 2018, pp. 1–6.

[29]. Poignonec T, Zanne P, Rosa B, and Nageotte F, “Towards in situ backlash estimation of continuum robots using an endoscopic camera,” IEEE Robotics and Automation Letters, vol. 5, no. 3, pp. 4788–4795, 2020.

[30]. Sefati S, Murphy R, Alambeigi F, Pozin M, Iordachita I, Taylor R, and Armand M, “Fbg-based control of a continuum manipulator interacting with obstacles,” in Intelligent Robots and Systems (IROS), 2018 IEEE/RSJ Int. Conference, 2018, pp. 1–7.

[31]. Wilkening P, Alambeigi F, Murphy RJ, Taylor RH, and Armand M, “Development and experimental evaluation of concurrent control of a robotic arm and continuum manipulator for osteolytic lesion treatment,” IEEE robotics and automation letters, vol. 2, no. 3, pp. 1625–1631, 2017. [PubMed: 29423447]

[32]. Shim V, Boheme J, Josten C, and Anderson I, “Use of polyurethane foam in orthopaedic biomechanical experimentation and simulation,” Polyurethane, pp. 171–200, 2012.

[33]. Monet F, Sefati S, Lorre P, Poiffaut A, Kadoury S, Armand M, Iordachita I, and Kashyap R, “High-resolution optical fiber shape sensing of continuum robots: A comparative study,” in 2020 International Conference on Robotics and Automation. IEEE, 2020, pp. 1–7.

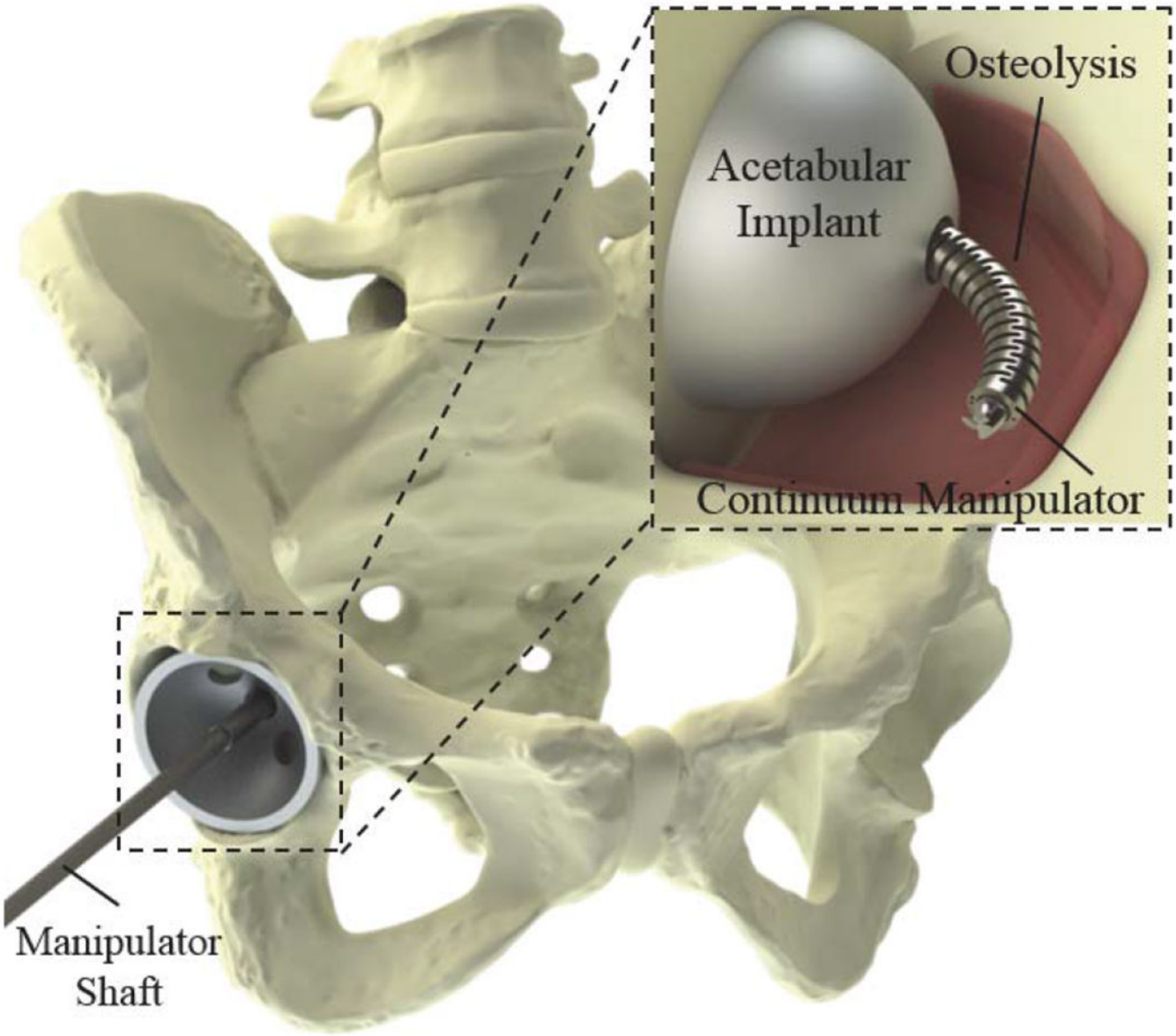

Fig. 1.

Robot-assisted treatment of Osteolysis. The continuum manipulator developed for orthopaedic applications equipped with flexible instruments inserted through a screw hole of the acetabular implant.

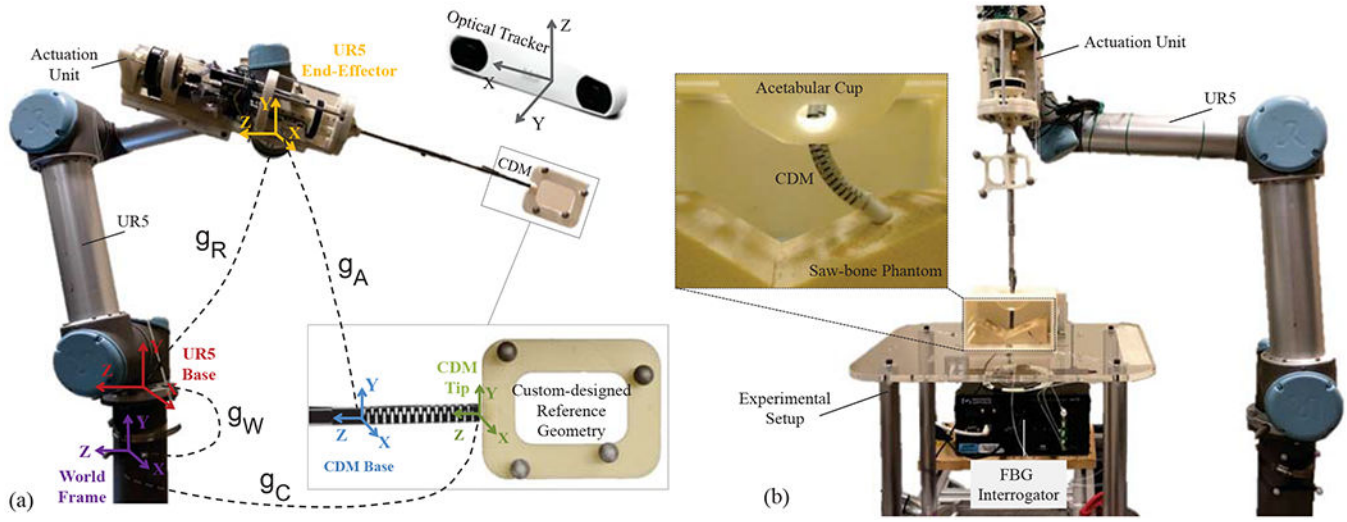

Fig. 2.

(a) Redundant surgical system and the custom-designed optical tracker reference geometry used for hand-eye calibration and training the data-driven algorithm for FBG sensing, (b) system during cutting of saw-bone phantom behind the acetabular cup component using flexible debriding tools.

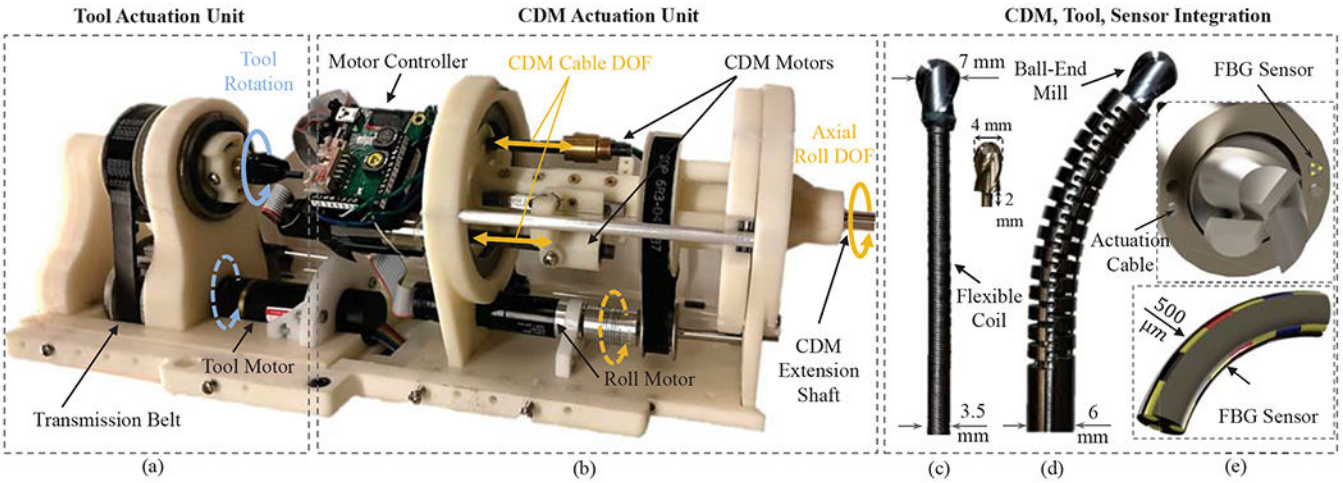

Fig. 3.

(a) Tool actuation unit comprised of a DC motor and transmission belt with collet clamping mechanism that holds the tool shaft, (b) the CDM actuation unit comprised of the three DC motors, one for axial roll motion and two for CDM actuation, with the two CDM cable DOFs and the axial roll DOF demonstrated in solid orange arrows, (c) flexible cutting/debriding tool comprised of a flexible torque coil and ball-end mill, (d) tool integration into the CDM, and (e) CDM tip view demonstrating the actuation cables and the FBG sensor.

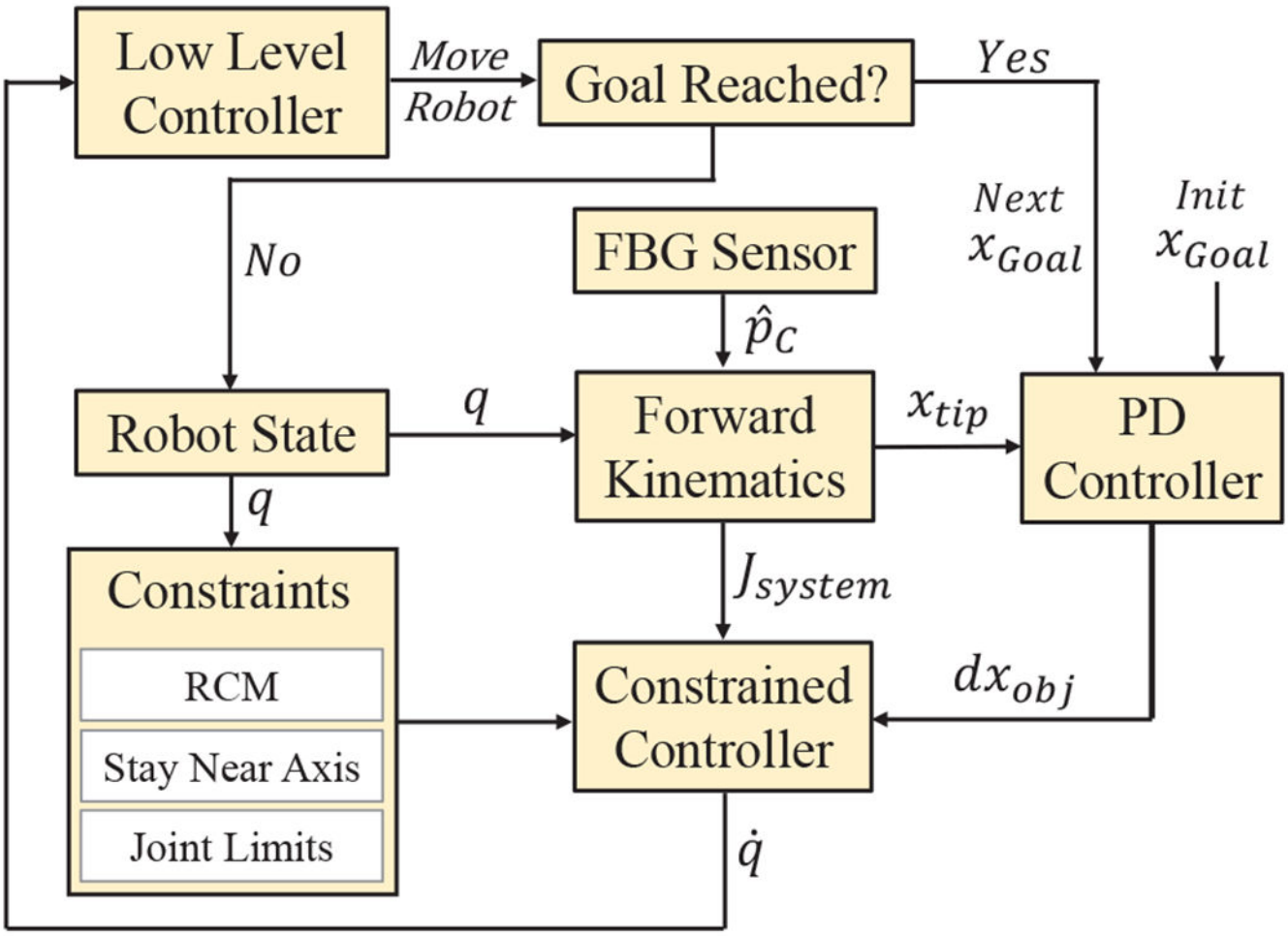

Fig. 4.
Block diagram for the closed-loop system.

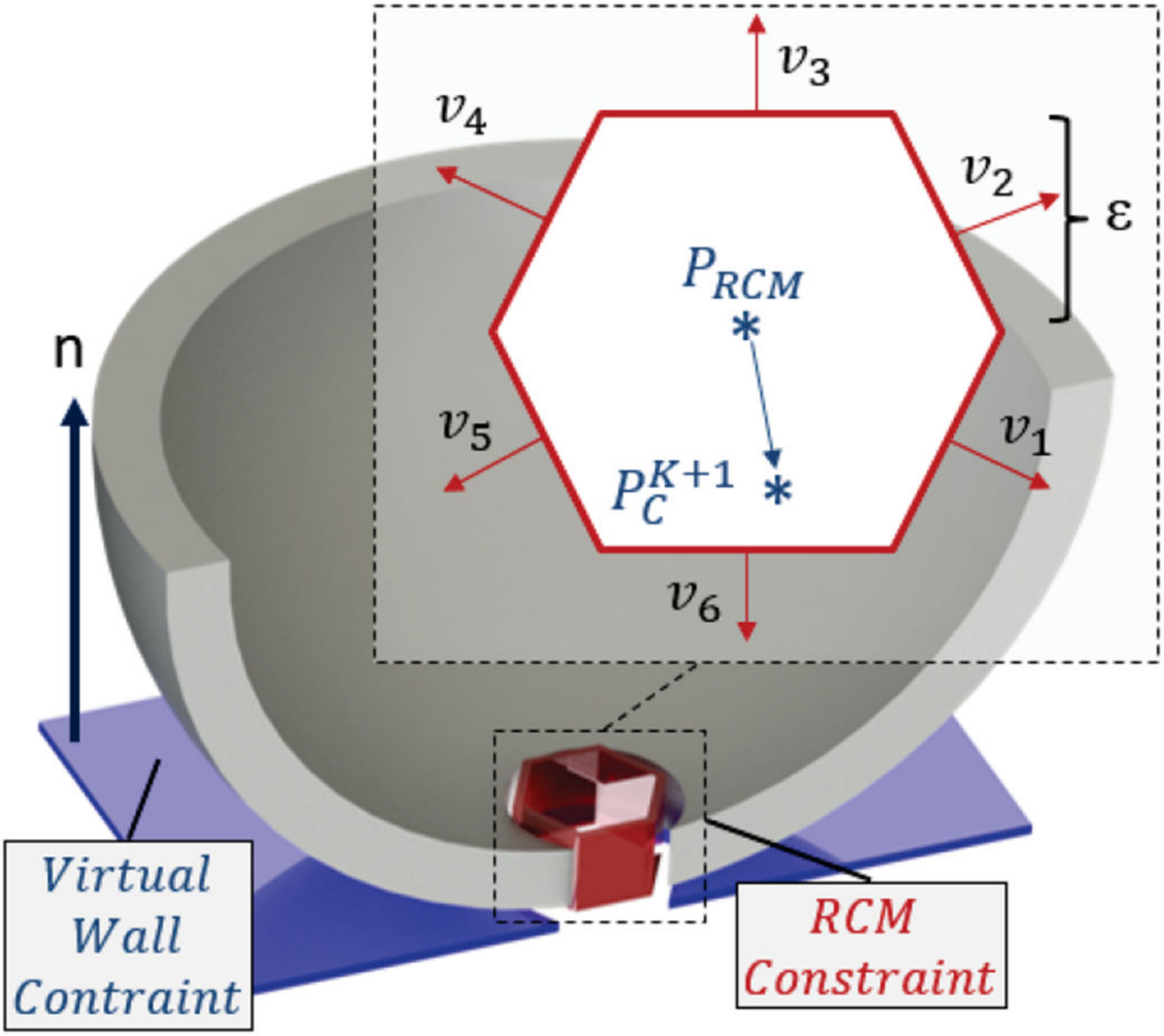

Fig. 5.
RCM constraint and the prism approximation with arbitrary number of faces (e.g. n=6), approximating the RCM allowed region

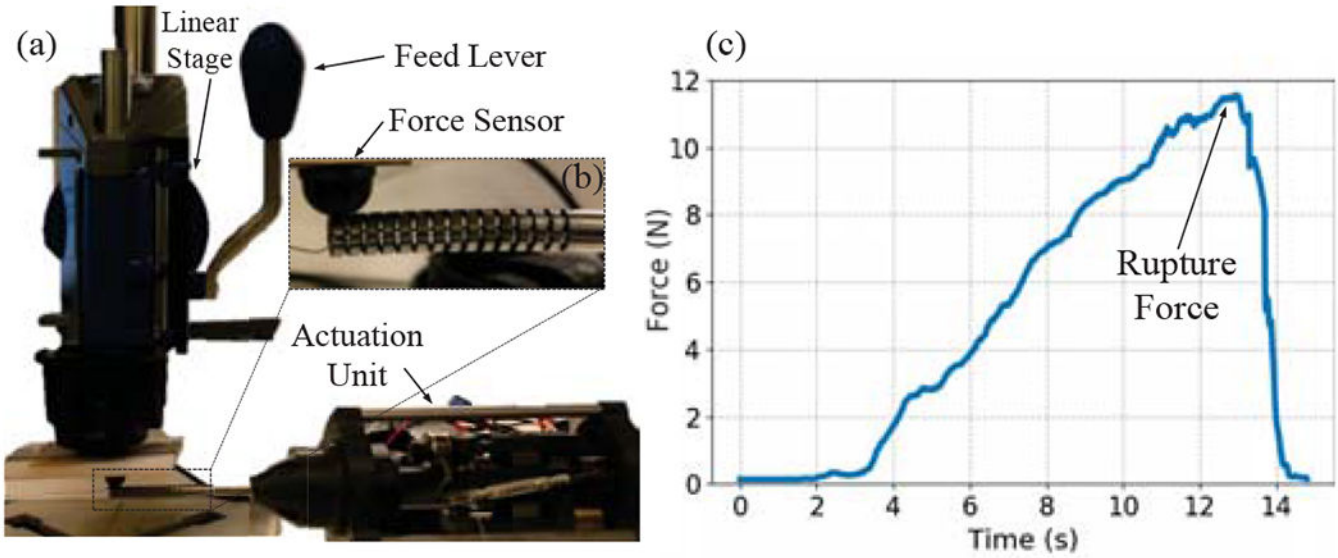

Fig. 6.

(a) Force testing experimental setup, (b) close-up view demonstrating the force sensor and the CDM, (c) end-effector force testing result during exertion of out-of-plane distal-end force.

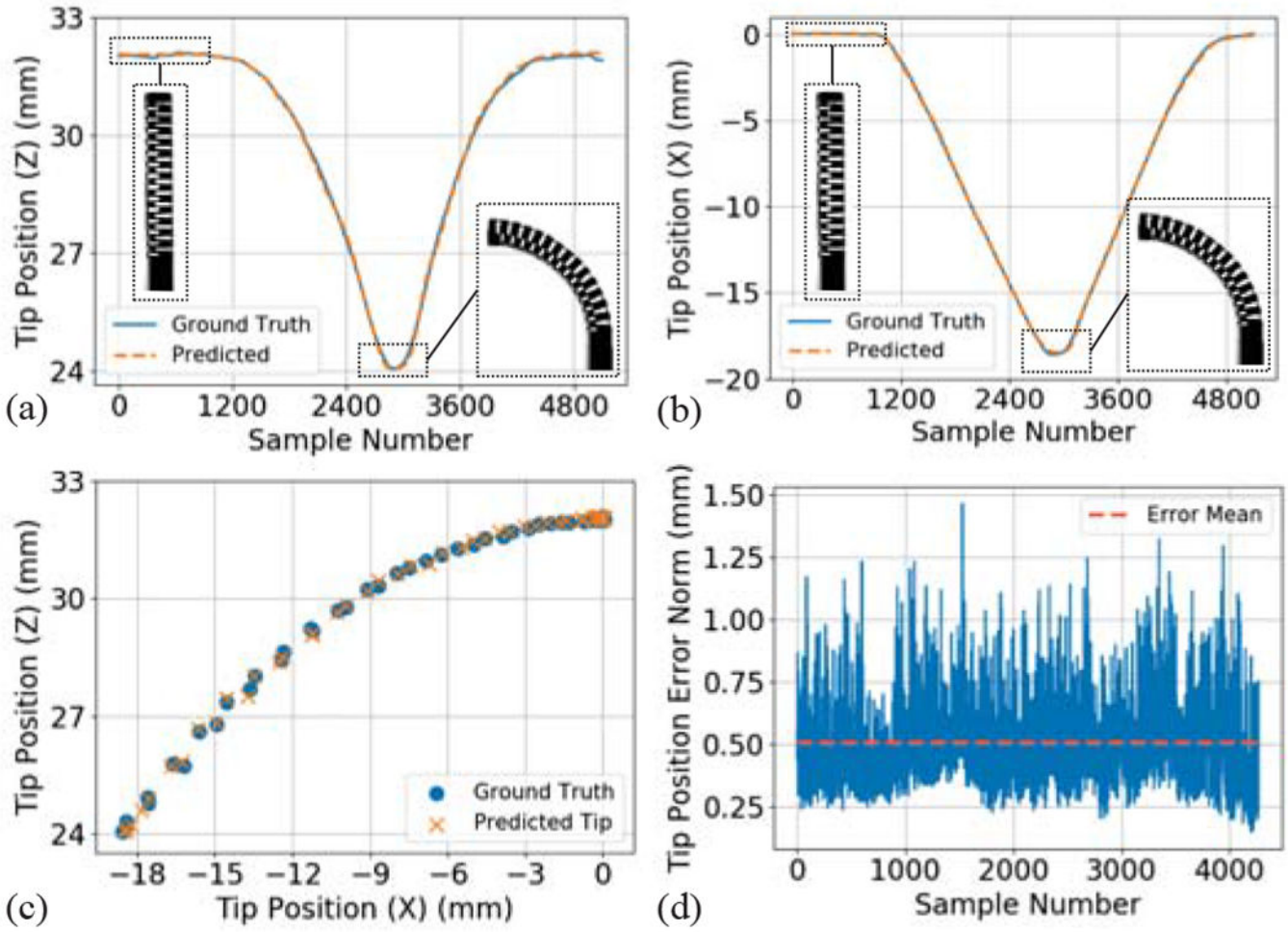

Fig. 7.

Comparison of the ground truth CDM tip position from the optical tracker and the estimation from the FBG data-driven approach in (a) direction Z; (b) direction X; (c) in 2-D plane; (d) system (CDM and robot) feedback accuracy (CDM TPE error with respect to the base of the entire system)

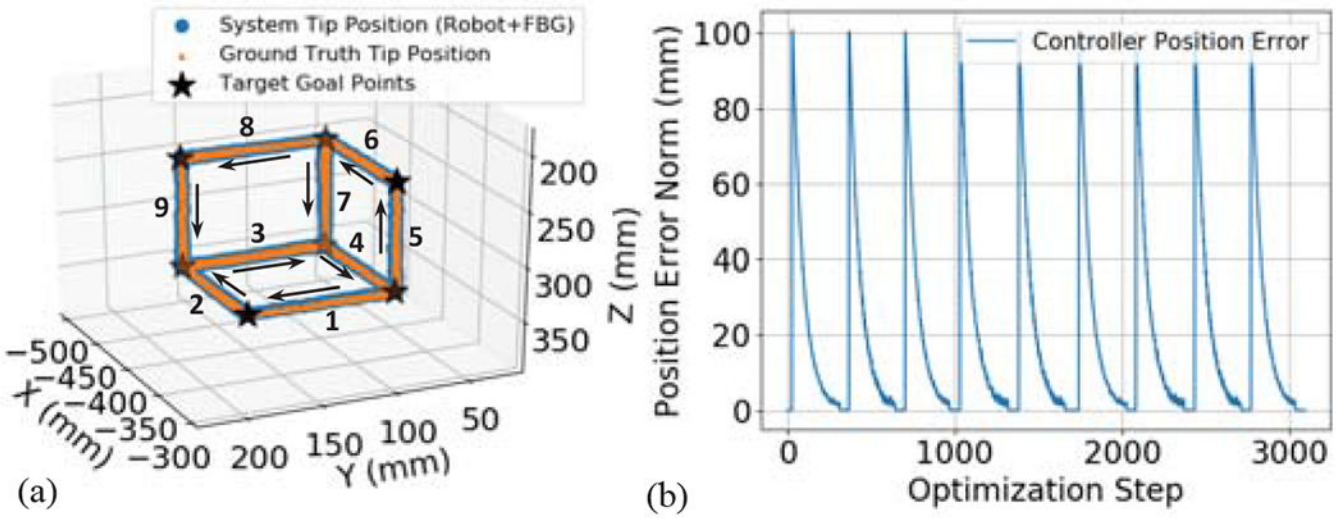

Fig. 8.

(a) Controller performance in reaching the seven corners of a 100 mm edge cube in space as goal points; (b) controller position error when reaching the cube corners (order of traced edges shown in (a)).

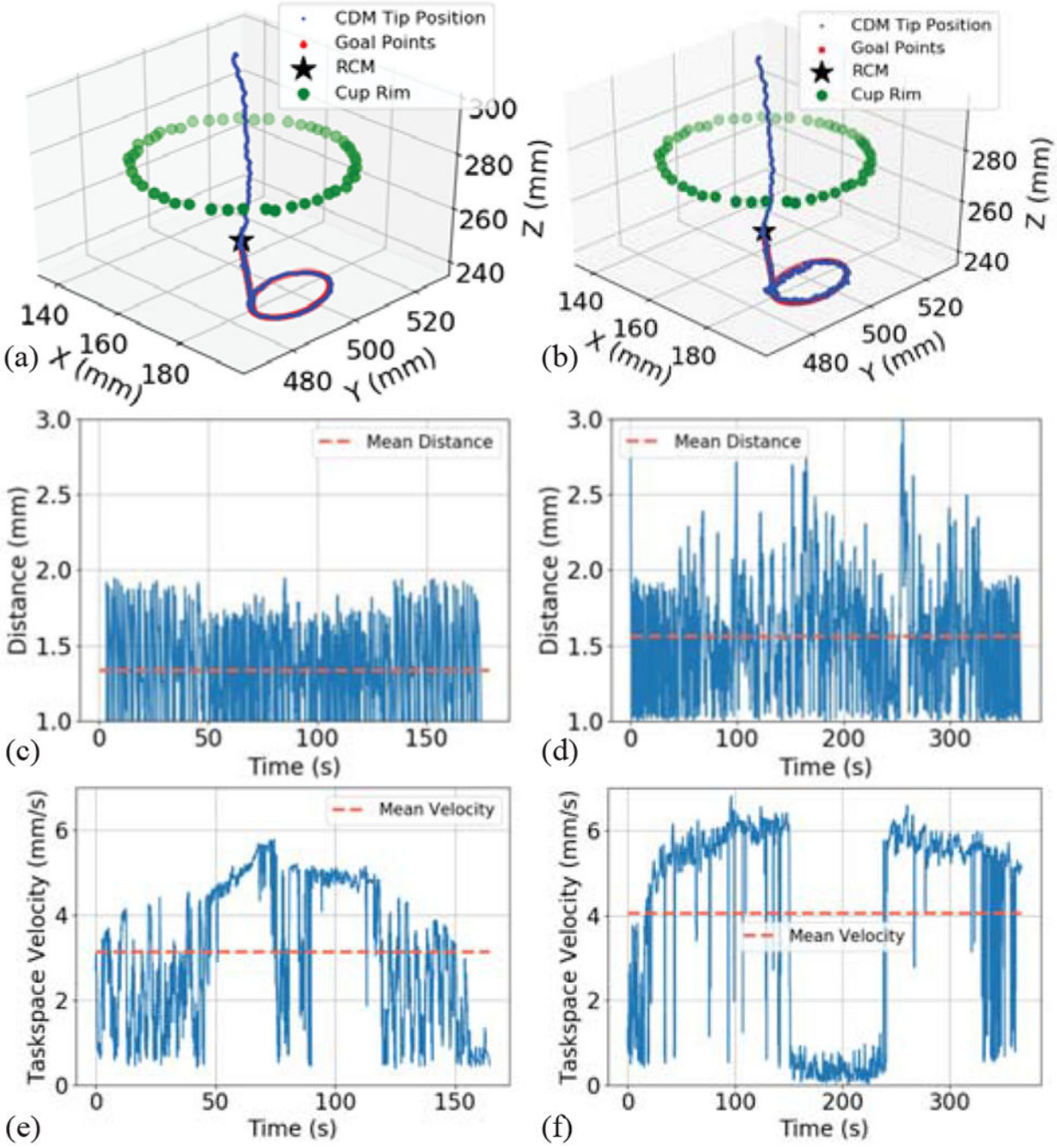

Fig. 9.

Controller performance in tracing a digitized circle behind the cup with constraints inactive (left figures) and active (right figures). (a) and (b) the desired cutting trajectory and the tracked CDM tip position; (c) and (d) CDM tip distance from the target points during cutting; (e) and (f) the generated task-space velocity.

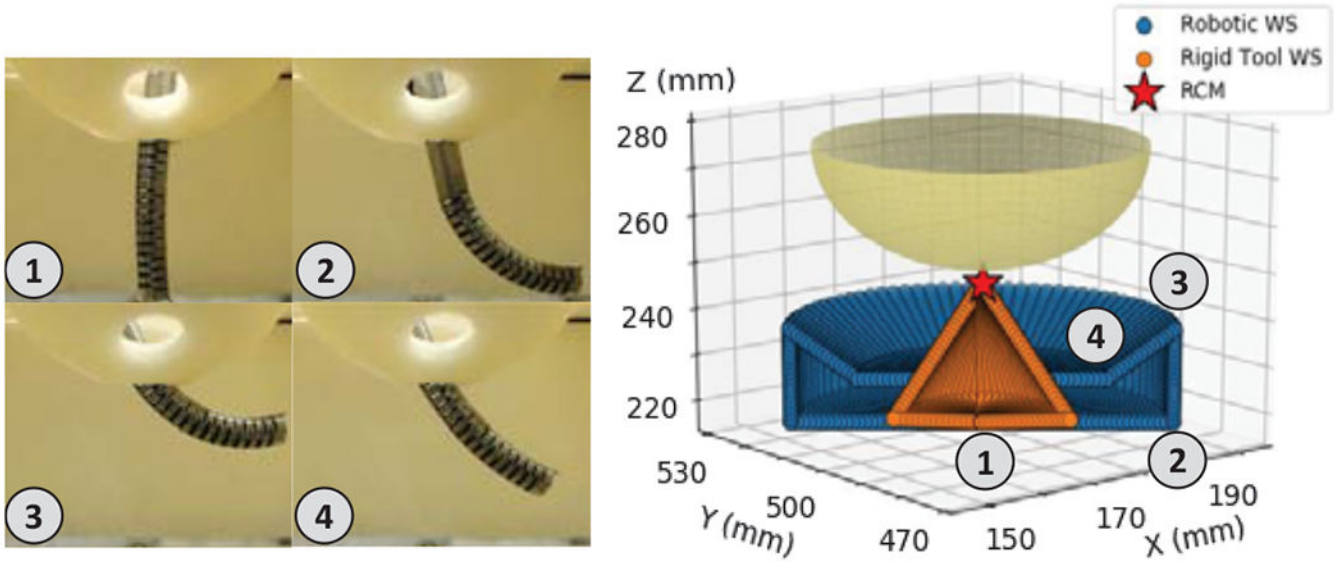

Fig. 10.

Workspace comparison between the conventional rigid-tool and the proposed robotic system in less-invasive treatment of osteolysis. Numbers indicate the state of the CDM behind the cup at workspace boundary points.

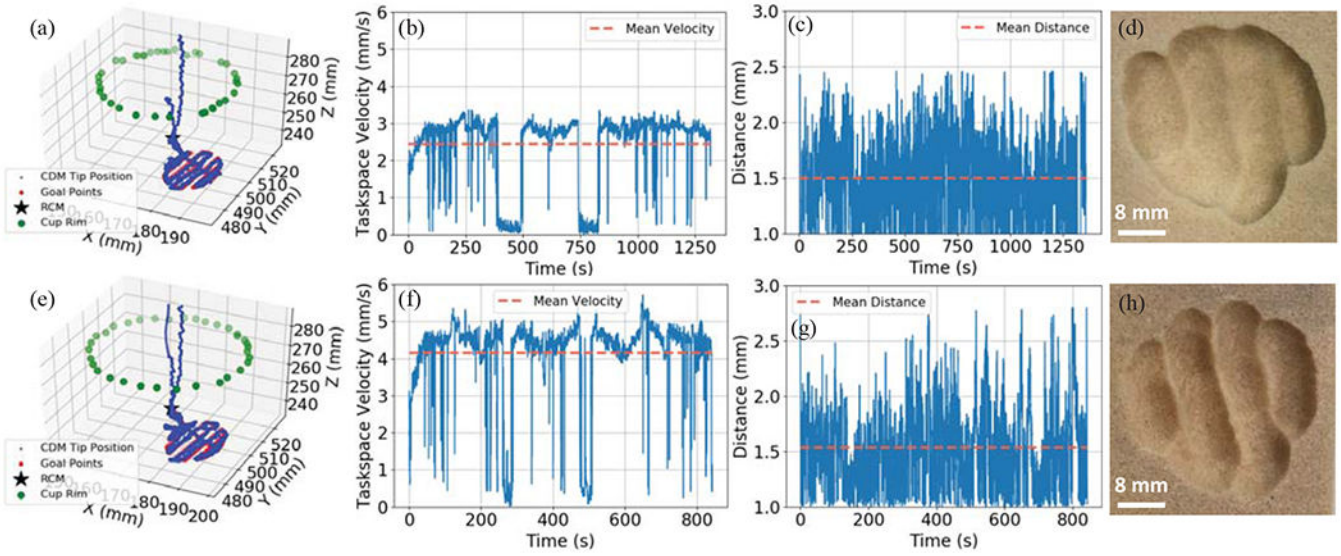

Fig. 11.

The cutting performance for saw-bone phantom PCF 10 (top row) and PCF 15 (bottom row). (a) and (e) the desired cutting trajectory and the tracked CDM tip position; (b) and (f) the generated task-space velocity; (c) and (g) CDM tip distance from the target points during cutting; (d) and (h) the resulting cutting trajectory on the surface for the two phantoms.

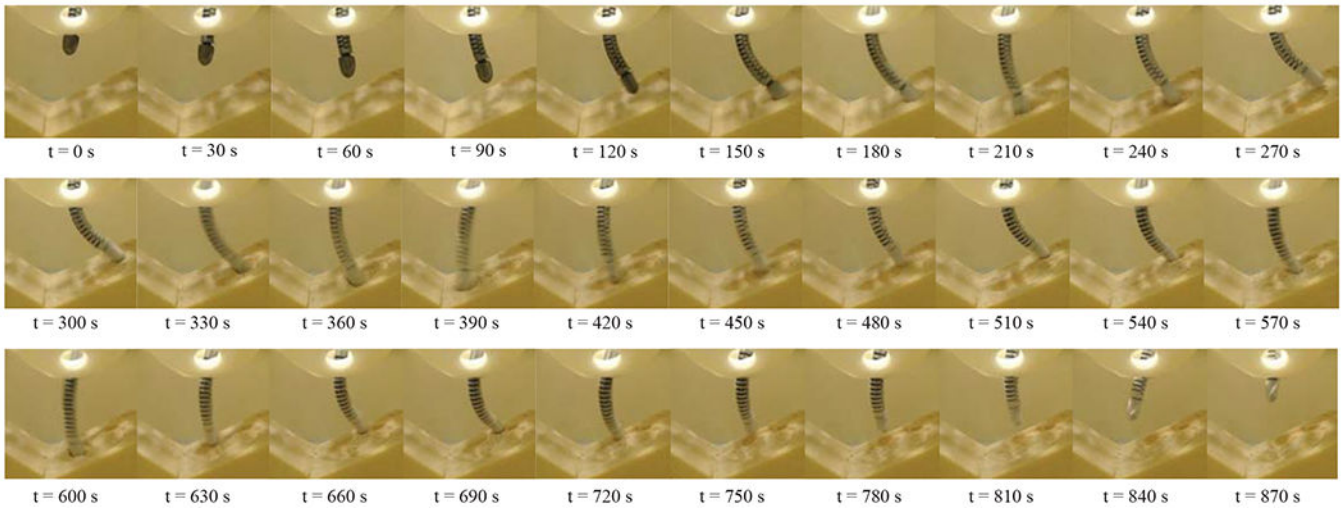

Fig. 12.

Snapshots of the CDM insertion into the acetabular cup component and cutting of the PCF 10 saw-bone phantom based on the planned trajectory.

TABLE I

CONTROLLER PERFORMANCE IN FREE ENVIRONMENT AND DURING CUTTING

		Distance (mm)		
	Constraints	**Mean**	**Std. Dev.**	**Max**
Free Environment	off	1.33	0.37	1.94
Free Environment	on	1.52	0.42	2.98
Cutting (PCF 10)	on	1.50	0.37	2.46
Cutting (PCF 15)	on	1.41	0.53	2.80